IRANIAN JOURNAL OF CATALYSIS

Properties of sol-gel synthesized multiphase TiO₂ (AB)-ZnO (ZW) semiconductor nanostructure: An effective catalyst for methylene blue dye degradation

Manikandan Balakrishnan, Rita John*

Department of Theoretical Physics, University of Madras, Guindy Campus, Chennai, India.

ABSTRACT

The present study, describes the structural, electrical, and the photocatalytic activity of sol-gel synthesized TiO₂- ZnO nanostructure. The synthesized mixed oxide nanostructure is characterized by XRD, FTIR, Raman, UV-Vis, FESEM, DLS and Impedance Spectroscopy analyses. In addition, photocatalytic activity of multiphase TiO₂ (TAB)-ZnO (ZW) nanostructure is analysed using Methylene Blue dye as the model dye under UV and Visible light illumination. The XRD analysis confirms the bi-phase TiO₂ and mono-phase ZnO in the multiphase TiO₂-ZnO nanostructures. The average crystallite size of 33 nm has been estimated using Scherrer formula. The crystallite size and mechanical properties such as strain, stress, and other parameters are analysed using Williamson-Hall model. The FTIR spectrum shows the characteristics absorption peaks of TiO₂ and ZnO at 679.44 and 432.79 cm^{-1} respectively, and reveals the presence of TiO₂ and ZnO in the synthesized multiphase nanostructure. The optical band gap is calculated using Tauc relation with the data obtained from UV-Vis spectrometer. The calculated band gap value is 3.1 eV. The FESEM study shows the spherical morphology and the DLS analysis confirms the particle size is 433 nm. The presence of Ti-O and Zn–O stretching modes are confirmed from Raman spectrum. The electrical properties such as dielectric constant, dielectric loss, and ac conductivity are analysed from impedance data. The prepared multiphase TiO₂ (TAB)-ZnO (ZW) nanostructure shows better photocatalytic activity in both UV and visible light region. The rate constant has been calculated as 0.0083 and 0.0052 min^{-1} for UV and visible light irradiation.

Keywords: Sol-Gel; Multiphase TiO₂-ZnO; Williamson-Hall model; Stress-Strain analysis; Photocatalysis.

1. Introduction

Today, the entire world faces serious environmental crises causing many dreadful diseases due to waste water and other pollutants [1-3]. Drinking water and healthy environmental surroundings are expected to be the challenges for human beings in the near future[4] . In the last few decades, the researchers have been working on various semiconductor materials towards different environmental issues [5, 6]. It was suggested that these semiconductor materials play an important role in energy and environment treatment through photo responsive process of solar cells [7, 8], photocatalysis [9], and sensors [10-12]. The photocatalysis is a versatile, inexpensive and environmental friendly technique to decompose organic pollutants with the help of semiconductor materials as photocatalyst.

Titanium dioxide (TiO₂) and Zinc Oxide (ZnO) are well known wide band gap semiconductors that gained much attention due to their unique properties such as absence of toxicity, low cost, optoelectronic, photo electrochemical properties, and chemical stability under different conditions [13, 14]. Both ZnO and TiO₂ semiconductors have nearly equal band gaps of about 3.37 eV for ZnO [15-17] and 3.2 eV for anatase TiO₂ [13, 18], and are reported to have limited use in visible region [19].

The solar spectrum has more than 45 % visible light and only 5 % UV [20]. The photocatalytic degradation can be increased by using a wide range of UV and visible light spectrum, because degradation efficiency also depends on the generation of electron hole pairs [21-23]. The mixed semiconductors have different redox energy levels in conduction and valence bands that are favourable for the effective charge separation. Also enhance the life time of charge carries.

*Corresponding author.
Email: ritajohn.r@gmail.com (R. John)

In the recent years, many researchers focus on nanocomposite [14, 24], multiphase nanostructures [25, 26], and different metal and non-metal doping semiconductors [27-30] to consume both UV and visible light, eventually to increase the photocatalytic degradation. The multiphase TiO_2 (TAB)-ZnO (ZW) nanostructure also increases the free charge carries in the conduction band of TiO_2 and reduces the recombination of electrons and holes, through the creation of lattice defect and band offsetting [25]. The band offset depends on the energy gap between different materials, the presence of dipoles at the interface, effect of strain, and other parameters. Further, Literature survey reveals the structural properties using Williamson-Hall (W-H) model for multiphase semiconductor nanostructure is highly limited. Therefore, evaluating the structural property of the nanostructures in both Scherrer equation and Williamson-Hall model is the better way for finding the interrelations of structural parameters such as stress, strain, dislocation density and crystallite size.

In the past, many researchers prepared TiO_2-ZnO semiconductor nanostructure by various synthesis techniques like chemical bath deposition [31], spray pyrolysis [32, 33], co-precipitation [34, 35], sol-gel [36-39], and hydrothermal [40] methods. Amongst all, the sol-gel method is the simplest route to synthesize nanoscale materials due to its merits of homogeneity, controlled temperature, and cost effectiveness[41, 42]. Hence in the present work, the sol-gel route is used to synthesize the multiphase TiO_2 (TAB)-ZnO (ZW) nanostructure. The morphology, structural, optical and electrical properties of synthesized multiphase nanostructure have been analysed by various analytical techniques: X-ray diffraction, FTIR, Raman, UV-Vis, Impedance, FESEM/EDX, and DLS. The inter relationship between lattice strain with crystallite size and dislocation density are analysed. In addition, the photocatalytic behaviour is also studied by using methylene blue (MB) as model dye to evaluate photocatalytic activity of multiphase TiO_2 (TAB)-ZnO (ZW) nanostructure.

2. Experimental

2.1. Materials

Titanyl acetylacetonate ($C_{10}H_{14}O_5Ti$, 99.5 % Purity), Zinc acetate ($C_4H_6O_4Zn.2H_2O$, 99 % purity), Ethanol (Analytical Reagent, 99.9% purity), NaOH and De-ionised water (Laboratory Reagent).

2.2. Preparation

1.31 g of Titanyl acetylacetonate and 1.10 g of Zinc acetate are taken separately along with 50 mL of ethanol. Each solution is stirred for 40 min with a magnetic stirrer at 60°C temperature. After 40 min, the mixture of Zinc acetate and ethanol are transferred into the sol solution of Titanyl acetylacetonate. The pH value of the solution is measured to be around 5 and 25 mL of DI water, which has been added to the above solution drop by drop to adjust the pH value of the base. The sol solution mixture (TZ) is again stirred continuously for 3 h to get the homogeneous gel with the temperature maintained at 80 °C. The gel is further kept to age overnight and washed several times with ethanol as well as de-ionised water. The obtained gel is dried and ground with agitate mortar. Finally, it was calcined at 500 °C for 4 h.

2.3. Characterization techniques

X-ray diffraction (XRD) measurement has been performed using powder X-ray diffractometer (SEIFERT JSO2002) equipped with monochromatic CuKα_1 radiation (λ = 0.15406 nm). FTIR spectrum is measured by using a Bruker FTIR spectrometer in the range of 400-4000 cm^{-1}. Raman spectroscopy (Nanophoton Raman-11, Japan) techniques are used for the analysis of Raman spectrum of multiphase TiO_2 (TAB)-ZnO (ZW) nanostructure. The absorption spectra are recorded using UV-Vis-NIR spectrometer (Varian, model 500). FESEM is used to examine the morphology of the prepared nanostructure and the elemental compositions are analysed using energy dispersive X-ray spectroscopy (model: HITACHI SU6600). The DLS particle size measurements are carried out using a Malvern instrument (ZEN3600). The computer-controlled Hewlett-Packard (model HP428A) electrochemical instrument is used to perform the Impedance analysis.

2.4. Photocatalytic degradation

The photocatalytic experiment was carried out in a 600 mL cylindrical vessel with an 8 W mercury vapour lamp (365 nm) placed along the axis of the vessel. The lamp was encased in a quartz glass tube to protect it from having direct contact with the aqueous solution. Reaction suspension is prepared by adding the required amount of photocatalyst into 500 mL of methylene blue solution with an initial concentration of 3×10^{-5} moles/litre. Prior to the photodegradation, the suspension is magnetically stirred in a dark condition for 30 min to establish adsorption–desorption equilibrium condition. The aqueous suspension containing methylene blue and photocatalyst are irradiated under

UV light with constant stirring. The analytic samples from the suspension are then collected at equal intervals of time, centrifuged, and filtered. The concentration of methylene blue is analysed by UV-Vis spectrometer at the wavelength of 664 nm.

3. Results and Discussion

3.1. X-Ray diffraction analysis

The structural properties of prepared TiO_2 (TAB)-ZnO (ZW) nanostructure are analysed using XRD spectrum as shown in Fig. 1. The obtained XRD pattern reveals the presence of TiO_2 (TAB)-ZnO (ZW) mixed oxides. The peaks at 25.30 (101), 36.98 (103), 37.75 (004), 48.03 (200), 53.78 (105), 54.86 (211), 55.06 (211), and 62.71 (204) clearly show the presence of tetragonal anatase TiO_2 structure and these diffraction peak values are matched well with JCPDS File # 78-2486 [43]. The peaks at 32.23 (100), 35.25 (002), 36.09 (101), 56.62 (110), and 63.37 (103) confirm the presence of hexagonal wurtzite ZnO in the prepared sample which is compared with JCPDS # 36-1451 [44]. Also, additional peaks are obtained at 30.42 (121), 58.15 (232), and 42.05 (221) corresponding to brookite phase in the mixed oxides system [45, 46]. The peaks obtained in this study clearly confirm the bi-phase TiO_2 (anatase+ brookite) and mono-phase ZnO (wurtzite) structures.

The crystallite size is calculated by using Scherrer method [47, 48], which is given by the equation (1).

$$\text{Crystallite Size } (D) = \frac{K\lambda}{\beta \cos \theta} \qquad (1)$$

where, D is the crystallite size in nm scale, K is shape factor which is equal to 0.94, λ is the wavelength of X-ray radiation $Cuk\alpha_1$ (λ = 1.5406 Å), β is the full width half maximum intensity (FWHM) and θ is the Bragg's angle.
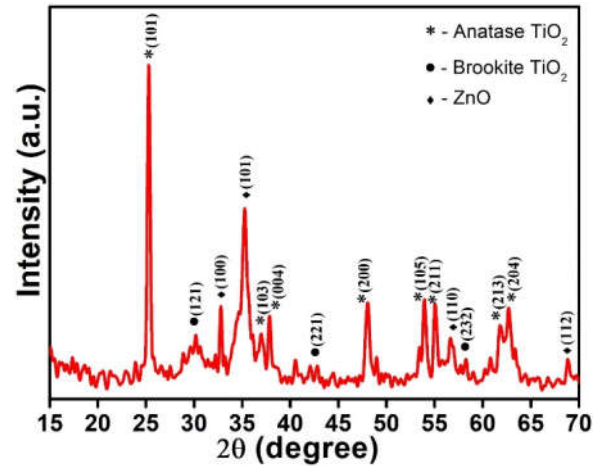
Fig. 1. The XRD pattern of multiphase TiO_2 (TAB)-ZnO (ZW) nanostructure.

The crystallite size is calculated using Scherrer formula for all the peaks and the obtained average crystallite size is 33 nm. The XRD pattern and the crystallite size clearly show that the crystallite size depends on various factors such as intensity, peak broadening, sharpness, dislocation density, and strain present in the materials. The dislocation density (δ) and strain (ε) are calculated using equation (2-3). The calculated crystallite size and other structural parameters are shown in Table 1.

$$\text{Dislocation density } (\delta) = \frac{1}{D^2} \qquad (2)$$

$$\text{Strain } (\varepsilon) = \beta_{hkl}/(4tan\theta) \qquad (3)$$

The variation of dislocation density and crystallite size with respect to strain is shown in Fig. 2. It clearly shows that the dislocation density increases as strain increases which in turn decreases the crystallite size. It also confirms that strain and dislocation density are directly influenced by the crystallite size.

Table 1. The structural parameters of multiphase TiO_2 (TAB)-ZnO (ZW) nanostructure

2θ (°)	(hkl)	FWHM (β) (°)	Crystallite size (D) (nm)	d-Spacing (Å)	Dislocation density (δ) $\times 10^{-3}$ nm^{-2}	Strain (ε) $\times 10^{-3}$
25.37	(101)	0.295	28	3.5173	3.4698	5.5167
30.25	(121)	0.109	78	2.9358	1.2687	1.7484
32.94	(100)	0.208	41	2.7746	2.4050	3.0091
36.09	(101)	0.495	17	2.4863	5.6882	4.8954
36.98	(103)	0.269	32	2.4286	3.0525	3.4189
37.84	(004)	0.265	33	2.3754	3.0220	3.2591
42.79	(221)	0.234	38	2.1470	2.6267	2.5721
48.17	(200)	0.693	13	1.8928	7.6277	6.7491
53.95	(105)	0.849	10	1.7000	9.1240	7.0809
55.10	(211)	0.419	22	1.6663	4.4782	3.4500
56.83	(110)	0.981	9	1.6242	10.4058	7.8206
5832	(232)	0.178	53	1.5850	1.8740	1.3858
61.92	(213)	0.099	97	1.5007	1.0102	7.0075
62.81	(204)	0.676	14	1.4802	6.9541	4.7789
68.78	(112)	0.561	17	1.3825	5.5803	3.5415
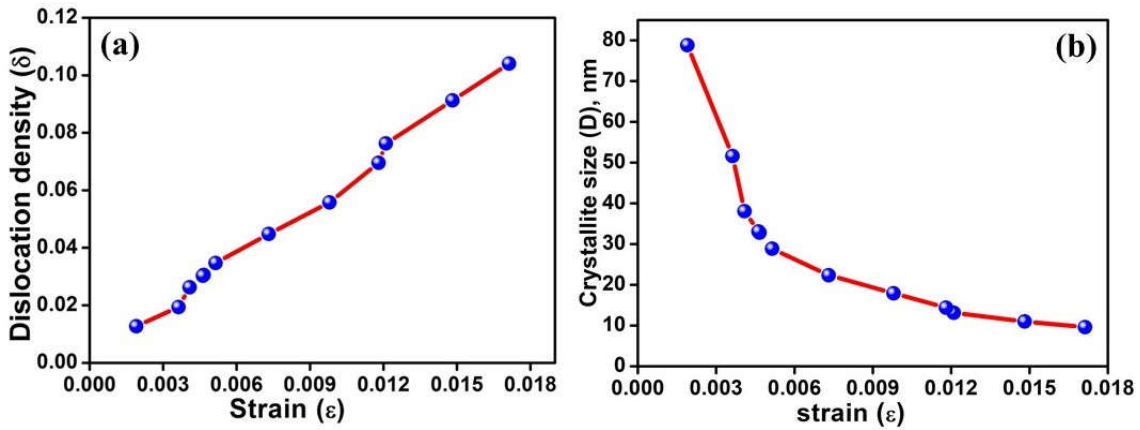
Fig. 2. Structural analysis: a) Variation of dislocation density with micro strain. b) effect of strain on crystallite size.

The peak broadens due to the presence of unequal strain in the materials, and plays an important role in the structural properties. The results clearly indicate that the discussion need**s** microstructural parameters for the better understanding of the behaviour of the prepared nanomaterial. In this respect, crystallite size, strain, and stress are also analysed using W-H model.

3.2. Williamson-Hall (W-H) model

The Williamson-Hall model is the simplest model to analyse the relation between crystallite size and strain. The crystallite size is effectively influenced by the strain induced line broadening. As strain increases the crystalline size tends to decrease which is confirmed from the obtained results. The equation (4) gives the relation between crystallite size and strain. The Williamson-Hall equations can be obtained by applying the Scherrer formula and strain parameter in equation (4). The equation (5) is known as W-H equation [49, 50] and this is called as the Uniform Deformation Model (UDM). In this model the crystal is considered to be isotropic, which undergoes uniform strain in all crystallographic directions.

$$\beta_{hkl} = \beta_D + \beta_{\varepsilon} \tag{4}$$

$$\beta_{hkl}cos\theta_{hkl} = \frac{K\lambda}{D} + 4\varepsilon sin\theta_{hkl} \tag{5}$$

where, β_D is due to the contribution of crystallite size, β_{ε} is due to the strain induced broadening, and β_{hkl} is the half maximum intensity of instrumental corrected broadening. It can be given by the following equation (6)

$$\beta_{hkl} = \left[(\beta_{hkl})^2_{measured} - (\beta_{hkl})^2_{instrumental}\right]^{1/2} \tag{6}$$

The crystallite size and strain can be estimated by taking the values of $\beta_{hkl}cos\theta_{hkl}$ and $4sin\theta_{hkl}$ along y-and x-axes respectively. The crystallite size is obtained from the intercept of resulted straight line and the slope of the linear fit gives the strain [51]. The UDM plot is shown in Fig. 3a. The consideration on the homogeneity and isotropic nature are not valid in all cases. Hence, the W-H equation is modified with the anisotropic strain and is known as the Uniform Stress Deformation Model (USDM). In this model, stress is assumed to be uniform in all crystallographic directions. This assumption is valid only for small strain. When strain is increased, the linear proportionality vanishes. The proportionality relation between stress and strain is observed from Hooke's law, which is given by $\sigma = \varepsilon Y_{hkl}$, where, σ represents stress, ε represents isotropic strain, and Y_{hkl} represents Young's modulus. Williamson-Hall equation is modified by substituting the value of ε in equation (5) when the particles deviate from its linearity due to strain, which is shown in equation (7). The plot between $\beta_{hkl}cos\theta_{hkl}$ and $\frac{4sin\theta}{Y_{hkl}}$ is shown in Fig. 3b, in which the slope of the linear fit and the y-intercept gives the stress and crystallite size respectively.

$$\beta_{hkl}cos\theta_{hkl} = \frac{K\lambda}{D} + \frac{4\sigma sin\theta}{Y_{hkl}} \tag{7}$$

Young's modulus for tetragonal [52] and hexagonal [50, 53] structures are calculated by using the following equations (8) and (9).

$$Y^{-1}_{hkl} = S_{11}(q_1)^4 + (q_2)^4 + S_{33}(q_3)^4 + (S_{44} + 2S_{13})((q_1)^2 + (q_2)^2)(q_3)^2 + (S_{66} + 2S_{12})q_1^2 q_2^2 \tag{8}$$

where, $q_1 = \left(\frac{h}{a}\right)d_{hkl}$, $q_2 = \left(\frac{h}{b}\right)d_{hkl}$,

$$q_3 = \left(\frac{h}{c}\right)d_{hkl}$$

S_{11}, S_{13}, S_{33}, S_{44}, S_{66}, and S_{12} are the elastic compliances of tetragonal TiO_2 structure and their corresponding values are $S_{11}= 4.91\times10^{-12}$, $S_{13}= -2.94\times10^{-12}$,
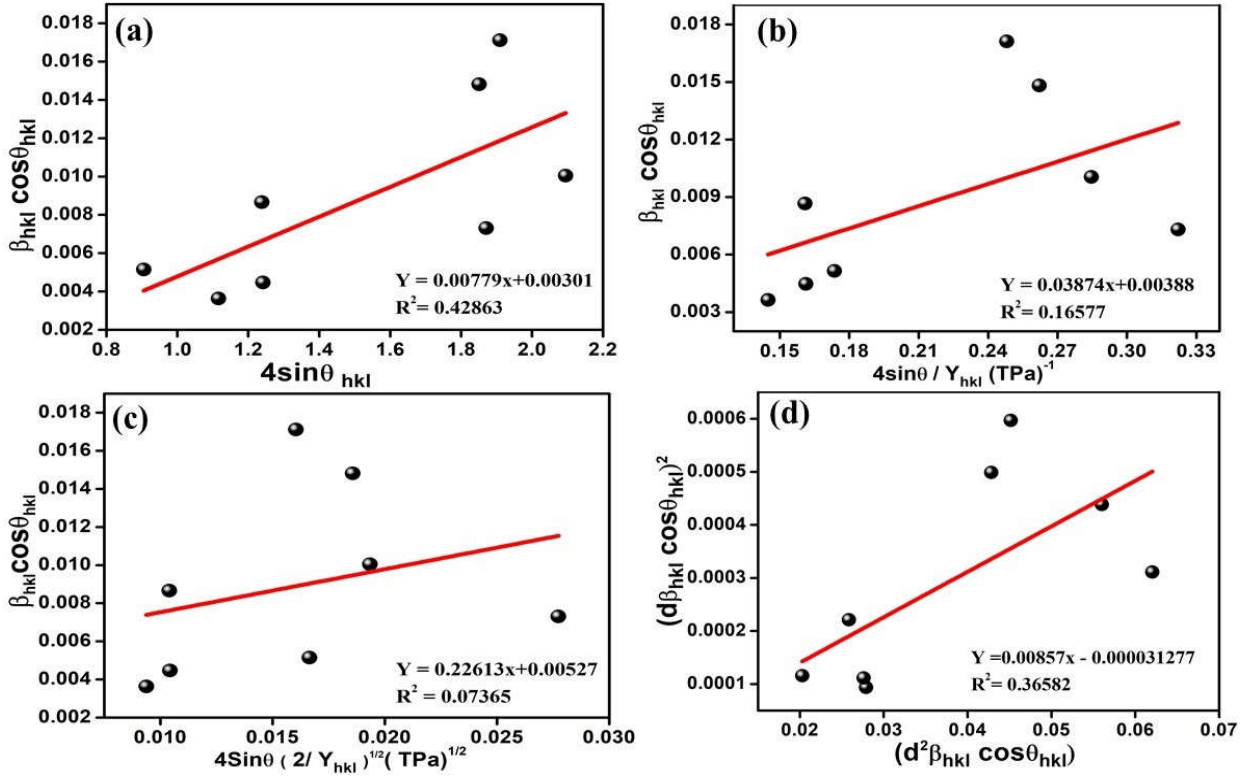
Fig. 3. Williamson-Hall (W-H) analysis: a) Plot for $\beta_{hkl} \cos\theta$ vs $4\sin\theta_{hkl}$. b) Plot for $\beta_{hkl} \cos\theta$ vs $4\sin\theta /Y_{hkl}$. c) Plot for $\beta_{hkl} \cos\theta$ vs $4sin\theta(\frac{2}{Y_{hkl}})$ ½. d) Plot for $(d^2_{hkl} \beta_{hkl}\cos\theta)$ vs $(d_{hkl} \beta_{hkl} \cos\theta_{hkl})^2$.

$S_{33}= 9.69\times10^{-12}$, $S_{44}= 18.5\times10^{-12}$, $S_{66}= 16.7\times10^{-12}$ and $S_{12}= -1.100\times10^{-12}$ m²N⁻¹ respectively.

$$Y_{hkl} = \frac{\left[h^2+\frac{(h+2k)^2}{3}+\left(\frac{al}{c}\right)^2\right]^2}{\left[S_{11}\left(h^2+\left\{\frac{(h+2k)^2}{3}\right\}\right)^2 + S_{33}\left(\frac{al}{c}\right)^4 +(2S_{13}+S_{44})\left(h^2+\frac{(h+2k)^2}{3}+\left(\frac{al}{c}\right)^2\right)\right]} \quad (9)$$

where, S_{11}, S_{13}, S_{33}, and S_{44} are the elastic compliances of ZnO material and their corresponding values are $S_{11}= 7.858\times10^{-12}$, $S_{13}= -2.206\times10^{-12}$, $S_{33}= 6.940\times10^{-12}$, and $S_{44}= 23.57\times10^{-12}$ m²N⁻¹ respectively.

The proportionality constant between stress and strain is no longer independent, when energy density is considered. The energy density can be calculated with the help of Hooke's relation. This approach is called the Uniform Deformation Energy Density Model (UDEDM). If the energy density is given as a function of strain in equation (10), then equation (7) can be modified with energy and strain relation as shown in equation (11).

$$u_{ed} = \frac{\varepsilon^2 Y_{hkl}}{2} \quad (10)$$

$$\beta_{hkl}\cos\theta_{hkl}= \frac{K\lambda}{D} + 4sin\theta\left(\frac{2u_{ed}}{Y_{hkl}}\right)^{1/2} \quad (11)$$

The energy density value can be obtained from the plot between $\beta_{hkl}\cos\theta_{hkl}$ (x-axis) and $4sin\theta\left(\frac{2}{Y_{hkl}}\right)^{1/2}$ (y axis) which is shown in Fig. 3c.

In W–H method, it is also understood that the line broadening must be isotropic due to the strain contribution. The strain profile is calculated from Gaussian function and crystallite size from Lorentzian function [50]. They are given by equation (12).

$$(d\beta_{hkl}cos\theta_{hkl})^2 = \frac{1}{V_S}(d^2\beta_{hkl}cos\theta_{hkl}) + \frac{\varepsilon_a^2}{2} \quad (12)$$

where, d is the interplanar spacing, V_S is the apparent volume weighted average size, and ε_a is the apparent strain. The apparent strain can be related to root-mean square strain ε_{RMS} by using the equation (13).

$$\langle\varepsilon_{RMS}\rangle = \left(\frac{\varepsilon_a}{2\sqrt{2\pi}}\right) \quad (13)$$

Fig. 3d shows the Size-Strain Plot (SSP). If $(d^2\beta_{hkl}cos\theta_{hkl})$ is taken along x-axis and $(d\beta_{hkl}cos\theta_{hkl})^2$ along y-axis, then the averaged crystallite size can be obtained from the slope of the linear fit. The calculated values are consolidated in Table 2. The calculated average crystallite size using Scherrer formula and various modified forms of

Table 2. Geometric parameters of TiO₂ (TAB)-ZnO (ZW) nanostructure calcined at 500 °C.

Scherer Method		Williamson- Hall (W-H) model								Size-Strain Plot (SSP)		
		UDM		USDM			UDEDM					
D (nm)	ε in 10^{-3}	D (nm)	ε in 10^{-3}	D (nm)	ε in 10^{-3}	σ (MPa)	D (nm)	ε in 10^{-3}	σ (MPa)	u_{ed} (KJm^{-3})	D_V (nm)	ε_a in 10^{-3}	ε_{RMS} in 10^{-3}
33.99	5.54	30.10	7.79	38.89	3.87	8.25	52.70	3.09	0.23	35.03	85.70	0.14	0.034

Williamson-Hall analysis such as UDM, UDSM, and UDEDM show a small variation, while considering the effect due to strain. This is due to the difference in average particle size distribution. The obtained results imply that the addition of strain in several forms has a very small effect on the average crystallite size.

3.3. FTIR analysis

Fourier Transform Infrared Spectroscopy is used to study the absorption of surfactant molecule at the TiO₂ surface. Fig. 4 shows the FTIR spectrum of multiphase TiO₂ (TAB)-ZnO (ZW) nanostructure, which is obtained in the range of 400-4000 cm⁻¹. The FTIR spectrum is a combination of functional group and fingerprint region. Oxides give absorption bands in the fingerprint region. The bands at 432.79 cm⁻¹ and 679.44 cm⁻¹ are the characteristic stretching modes of ZnO and TiO₂ nanoparticles respectively [54]. The absorption peaks around 1367.45 cm⁻¹ and 1707.52 cm⁻¹ are due to the stretching and bending vibrations of water molecule and carbonyl respectively [55]. The band located at 2344.53 cm⁻¹ is due to the presence of atmospheric CO₂ in the instrument and the band located at 2638.20 cm⁻¹ is attributed to the C-H stretching vibration [56, 57]. The obtained results clearly show the presence of Ti–O stretching mode, Zn-O stretching, water molecule and OH groups.
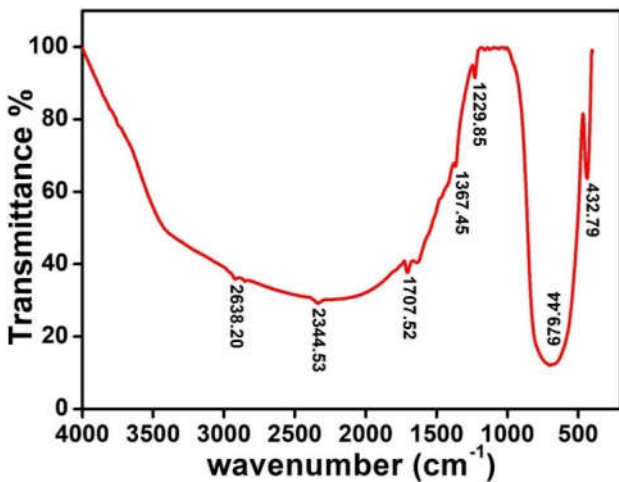
3.4. Optical analysis

The absorption spectrum of TiO₂ (TAB)-ZnO (ZW) multiphase nanoparticles is analysed using UV-Vis spectroscopy, which is shown in Fig. 5. The absorption peak is observed at 308 nm and the optical band gap of TiO₂ (TAB)-ZnO (ZW) multiphase nanostructure is calculated using Tauc relation, which is given by the following Kubelka-Munk equation (14).

$$(\alpha h\nu) = C\left(h\nu - E_g\right)^n \tag{14}$$

where, E_g is the optical band gap of the semiconductor (E_g *in eV*), α is the absorption coefficient (defined from Beer-Lambert's law), $h\nu$ is the energy of incident photons (h Planck's constant in Js, ν is light frequency in s⁻¹), C is the absorption constant, and n depends on the different types of transitions [58]. The transition values of direct band, indirect band, forbidden direct band, and forbidden indirect band are 1/2 , 2, 3/2, and 3 respectively [59, 60]. The band gap is determined from the Tauc plot, which is plotted between hν (eV) and $(\alpha h\nu)^{1/2}$ (cm⁻¹eV)², and the calculated band gap value is 3.1 eV. The obtained absorption edge and optical band gap indicate red shift for multiphase semiconductor catalyst, which clearly shows that it can be used as a catalyst under both UV and Visible light irradiation.

Fig. 4. FTIR spectrum of multiphase TiO₂ (TAB)-ZnO (ZW) nanostructure.
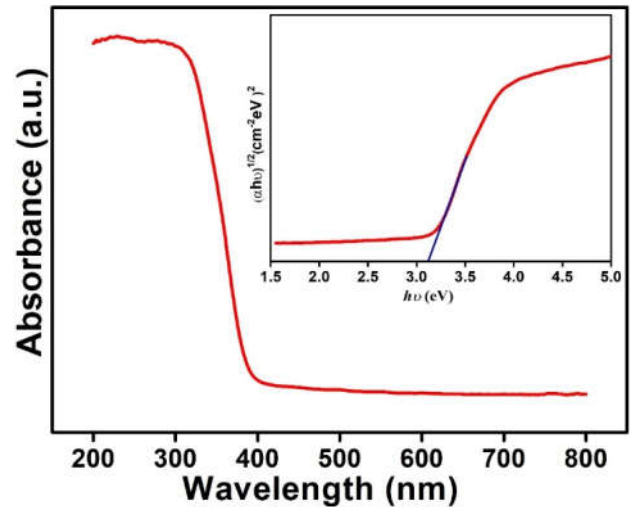
Fig. 5. UV-Visible spectrum of multiphase TiO₂ (TAB) - ZnO (ZW) nanostructure.

In addition, the conduction (E_{CB}) and valence (E_{VB}) band edge potentials are calculated using the following equations (15 and 16)

$$E_{VB} = X - E_e + \frac{1}{2}E_g \qquad (15)$$

$$E_{CB} = E_{VB} - E_g \qquad (16)$$

where, X is the geometric mean of the electronegativity of constituent atoms in the semiconductor, which is defined as the arithmetic mean of the atomic electron affinity and the first ionization energy; E_e is the free electron energy on the hydrogen scale (about 4.5 eV), and E_g is the band gap [61]. The calculated conduction band (E_{CB}) and valence band (E_{VB}) potentials for TiO_2 (TAB)-ZnO (ZW) multiphase semiconductor are -0.30 and + 2.79 eV respectively.

3.5. Raman analysis

The Raman spectrum of TiO_2 (TAB)-ZnO (ZW) multiphase oxides is shown in Fig. 6 and the multiphase nanostructure oxide system is also confirmed from the obtained Raman bands. The Raman bands are characterized based on six different factor group analysis for anatase TiO_2 [62]. The vibration modes have been following representations$\left(1A_{1g} + 2B_{1g} + 3E_g\right)$ at 140, 196, 395, 512, and 635 cm^{-1}. Among these representations, 140, 196, and 395 cm^{-1} are assigned to E_g mode. The 635 cm^{-1} to A_{1g} mode and 512 cm^{-1} to unresolved doublet mode. The additional bands observed at 225 and 339 cm^{-1}correspond to E_2 mode of zinc sublattice and oxygen respectively. E_2 mode corresponds to non-polar phonons, which exhibits two frequencies for oxygen and zinc atoms. E_2 (high) is assigned to oxygen atom and E_2 (low) is assigned to zinc sublattice [63].
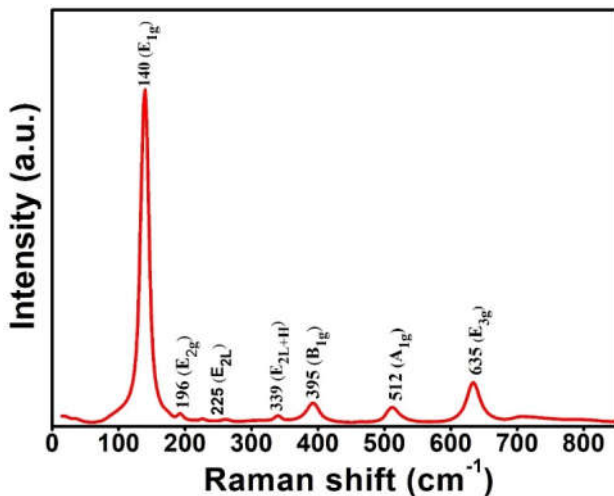
Fig. 6. Raman spectra of TiO_2 (TAB)-ZnO (ZW) multiphase nanostructure.

3.6. Morphology analysis

The surface morphology of the prepared TiO_2 (TAB)-ZnO (ZW) mixed oxides is examined using Field Emission Scanning Electron Microscopy (FESEM), which is shown in Fig. 7. The FESEM photographs are taken for different magnifications and the obtained result shows that the particles are spherical in shape. The elemental composition of the prepared mixed oxides sample is carried out by EDX. The obtained spectrum is shown in Fig. 8, which confirms the presence of Ti, O, and Zn elements in the prepared TiO_2 (TAB)-ZnO (ZW) nanostructure.

3.7. DLS analysis

The Dynamic Light Scattering (DLS) and Zeta potential techniques are used to determine the particle size and stability of the prepared mixed oxide nanoparticles. Fig. 9 shows the particle size distribution and Zeta potential, which are carried out by DLS using Malvern Zeta sizer. The particle distribution graphs show two peaks with particle size 433 and 97 nm. The obtained particle size using DLS study is in good agreement with the particle size obtained from FESEM. The Zeta potential gives the stability of the colloidal solution of the nanoparticles and these particles are said to be stable if its potential exists between -30 mV to +30 mV [64]. The Zeta potential obtained in this study is -0.0165 mV, which exists within the above-mentioned range and the results confirm that the prepared TiO_2 (TAB)-ZnO (ZW) mixed oxides have good stability.

3.8. Impedance analysis

The electrical properties of TiO_2 (TAB)-ZnO (ZW) nanostructure are analysed using Impedance Spectroscopy Technique (IS). The electrical conductivity of these materials depend on various parameters, such as crystallographic structure, compositions, polarization, and mechanical properties [65]. The experiment was conducted using 8 mm diameter pellet, by applying a pressure of 5 tons cm^{-2}. The Nyquist plot shown in Fig. 10, consists of real (Z') and imaginary (Z") components in a complex impedance plane. This is represented by the following equation.

$$Z^* = Z' + jZ'' \qquad (17)$$

were Z' and Z'' are real and imaginary parts of the complex impedance, it gives the contribution of resistance and capacitance due to grain and grain boundaries. The obtained Nyquist plot is in the form of a semicircle, which represents the electrical behaviour with respect to grain and grain boundary in the materials and the semicircle formed in the low frequency region corresponds to the contribution by grain boundary.
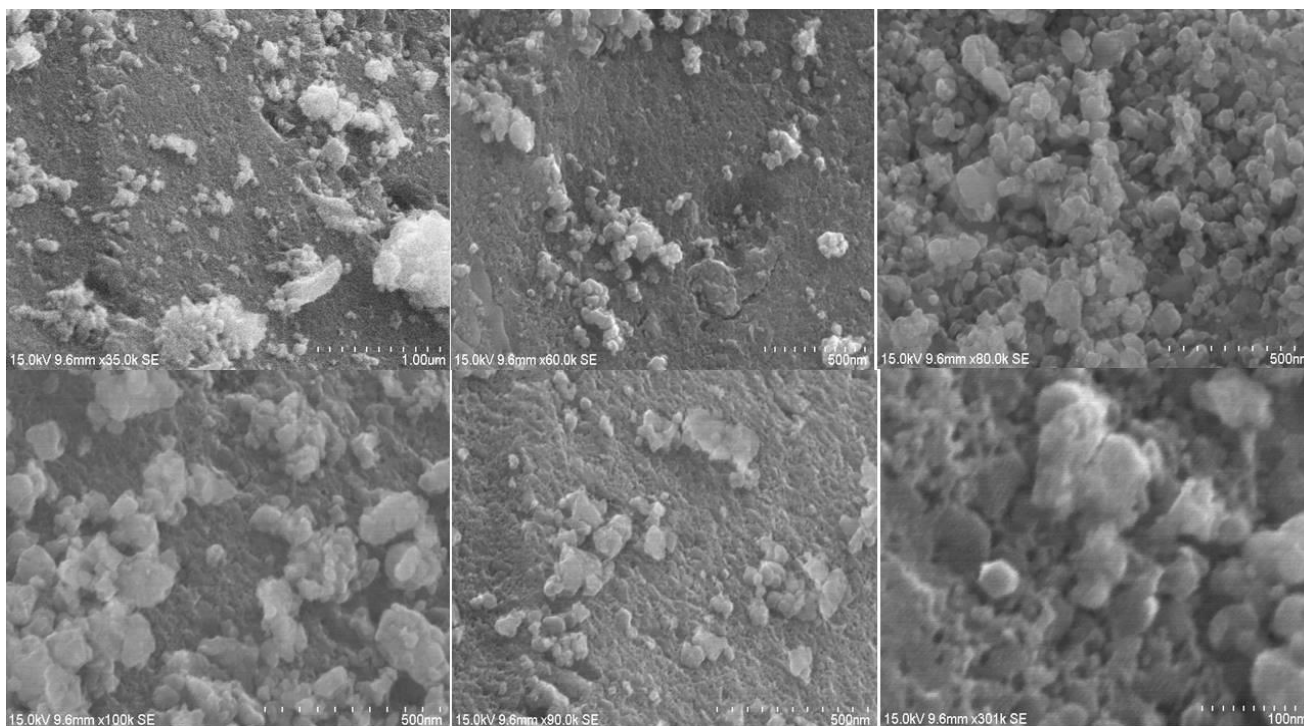
Fig. 7. FESEM images of TiO$_2$ (TAB)-ZnO (ZW) nanostructure.

Element	Weight%	Atomic%
O K	43.90	73.27
Ti K	25.61	14.27
Zn L	30.49	12.46
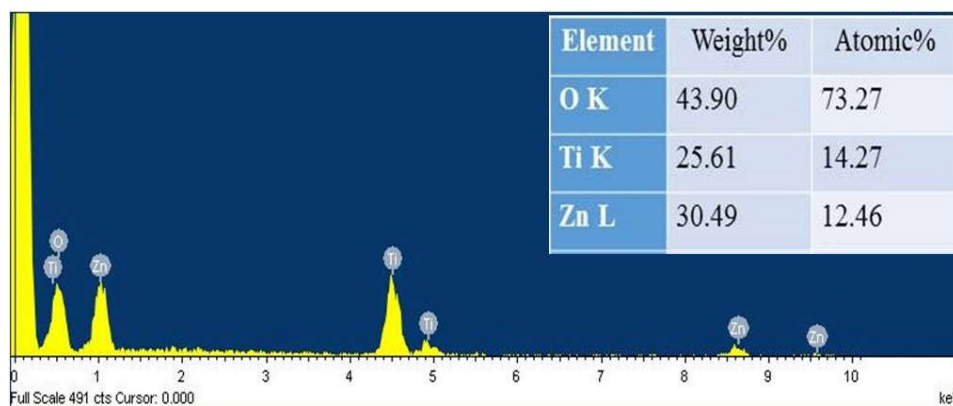
Fig. 8. EDX Spectrum of multiphaseTiO$_2$-ZnO nanostructure.
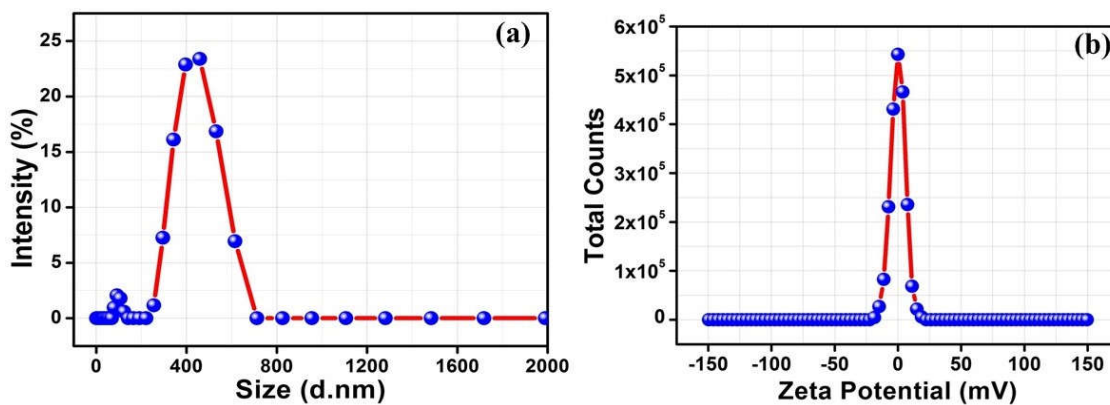
Fig. 9. DLS analysis of multiphase TiO$_2$ (TAB)-ZnO (ZW) nanostructure: a) Particle Size Distribution. b) Zeta potential.
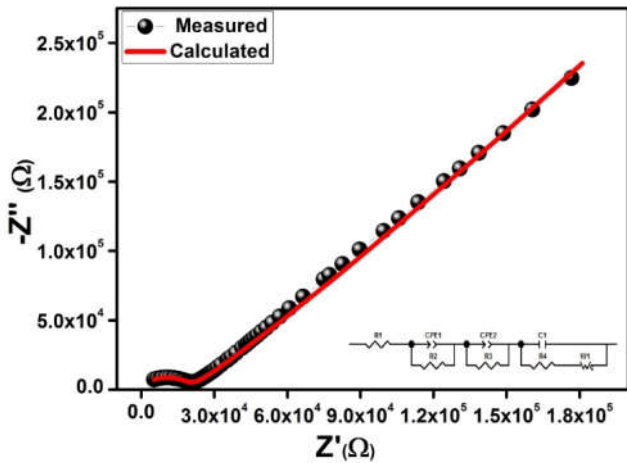
Fig. 10. Nyquist plots and equivalent circuit (inset) of multiphase TiO₂ (TAB)-ZnO(ZW) nanostructure.

The ZSim software has been used to model the semicircle in the impedance analysis. In the impedance spectrum, each semicircle can be fitted by using resistor (R) and capacitor (C) that are connected in parallel. The obtained Nyquist plot can be expressed in the form of Randles equivalent circuit, which is provided as inset in Fig. 10 and the simulated results of electrical components (R, C, etc.) are shown in Table 3. Fig. 11 shows the variations of real and imaginary parts of the complex plane with respect to frequency. The complex impedance values are higher at lower frequency and as the frequency increases, Z' and Z'' tend to decrease and become independent of temperature, which is due to the space charge polarization contributions.

Fig. 12 (a-e) shows the electrical behaviour of various parameters with respect to frequency such as dielectric response, electric modulus, and dielectric loss. The dielectric behaviour of TiO₂ (TAB)-ZnO (ZW) multiphase nanostructure is shown in Fig. 12 (a-b).
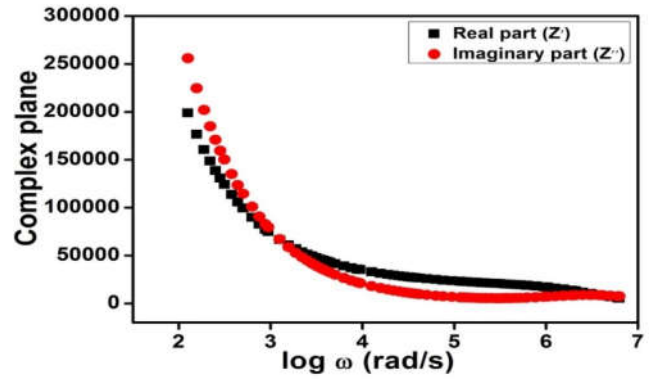
Fig. 11. The complex impedance of multiphase TiO₂ (TAB)-ZnO (ZW) nanostructure.

The dielectric behaviour of materials depends on various polarization effects, such as dipolar, atomic, electronic, and space charge polarizations [65]. The complex permittivity plotted against frequency clearly shows that both ε' and ε'' decrease with increasing frequency due to the contributions of electronic and atomic polarization effects. The dielectric response is higher at low frequency region due to charge accumulation at grain boundary which is in turn, due to the existence of space charge polarization. Fig. 12 (c-d) shows the real (M′) and imaginary (M″) electric modulus plot and both modulus spectra increases non-linearly with increasing frequency. The dielectric loss of TiO₂ (TAB) -ZnO (ZW) nanostructure is shown in Fig. 12e. The dielectric loss (tan δ) is an imaginary permittivity and describes energy dissipation in the materials due to domain wall resonance. The result obtained in the study indicates that the dielectric loss increases with increased frequency. The Fig. 13 (a-b) shows the AC conductivity with respect to frequency. The conductivity is a combination of AC and DC conductivities, which is given in the following equation.

Table 3. Electrical parameters of the equivalent circuit deduced from the impedance spectrum of TiO₂ (TAB)-ZnO (ZW) nanostructure.

Parameter	Calculated values
Resistances R_1, R_2, R_3, R_4	0.1 (Ω), 579.9 (kΩ), 298.2 (Ω), 19.48 (kΩ)
CPE_1, CPE_2	1.882×10^{-8} (F), 4.063×10^{-11} (F)
Capacitance (C_1)	2.253×10^{-8} (F)
Warburg (W_s)	4.063×10^{-7}
Chi-Squared	3.364×10^{-4}
Conductivity (σ_{ac})	0.50006 $(\Omega/cm)^{-1}$
Binding energy (ω_m)	0.3088 (eV)
Minimum hopping distance (R_m)	0.00295 (Å)
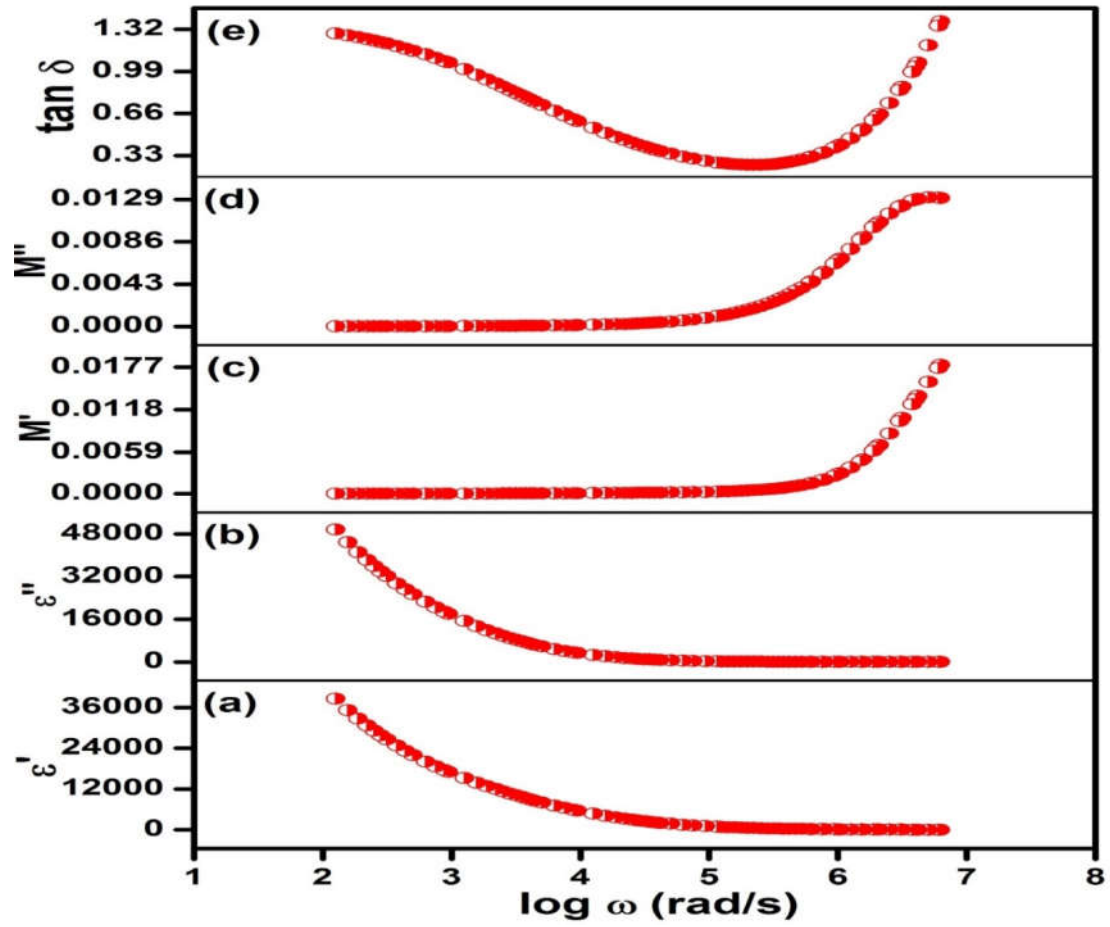
Fig. 12. Dielectric analysis of TiO$_2$ (TAB)-ZnO (ZW) multiphase nanostructures.

$$Y = 0.50006x - 10.4487$$
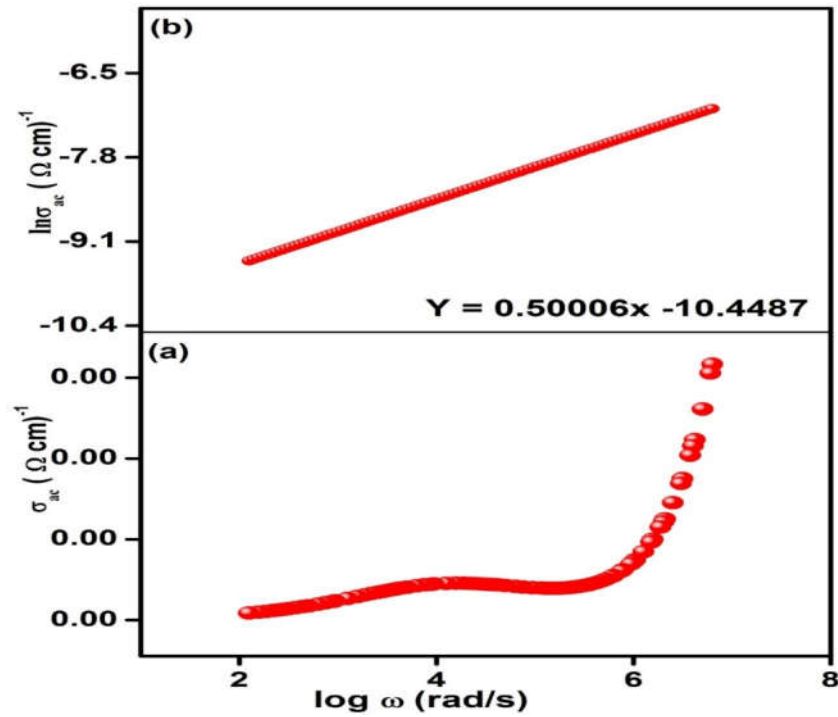
Fig. 13. The variations of ac conductivity with frequency.

The Fig. 13 (a-b) shows the AC conductivity with respect to frequency. The conductivity is a combination of AC and DC conductivities, which is given in the following equation.

$$\sigma = \sigma_0(T) + \varepsilon'\varepsilon_0\omega tan\delta\sigma0 \tag{18}$$

where, ω is the angular frequency, $\sigma_0(T)$ is the DC conductivity, ε' is dielectric constant, ε_0 is permittivity of free space (8.854×10^{-12}), and $tan\delta$ gives the dielectric loss.

The terms $\varepsilon'\varepsilon_0\omega tan\delta$ gives the AC conductivity, which depends on frequency but DC conductivity shows independent behaviour with frequency [65-68]. The obtained AC conductivity plot shows the frequency dependence behaviour, the conductivity increases with increasing frequency, which is due to the increase in electron hopping frequency and the conductivity becomes almost constant at low frequency region. The frequency dependent empirical formula of AC conductivity is given in equation (19).

$$\sigma_{ac}(\omega) = B\omega^n \tag{19}$$

where, n is a dimensionless constant, which has the value between 0 and 1, if n = 0, the conductivity is frequency independent and is called DC conductivity. If $n \leq 1$, then the conductivity becomes frequency dependent, which is called AC conductivity [67]. The value 'n' can be determined from the slope of the graph drawn between $ln\sigma_{ac}$ and frequency, which is shown in Fig. 13b and the obtained value of n is 0.50006. The binding energy and minimum hopping distance can be calculated using the combined barrier hopping model [69]. It is given by the following equations (20) and (21).

$$B_E = \frac{6K_\beta T}{\beta} \tag{20}$$

$$R_{minimum} = \frac{2e^2}{\pi\varepsilon\varepsilon_0 B_E} \tag{21}$$

where, B_E is the binding energy, ε is dielectric constant, ε_0 is permittivity of free space and $\beta = 1 - n$. The obtained values are given in Table (3).

3.9. Photocatalytic degradation of MB dye

The photocatalytic behaviour of the prepared multiphase TiO$_2$ (TAB)-ZnO (ZW) nanoparticles is studied using methylene blue as a model dye. Methylene blue is one of the hazardous organic dye which causes many environmental and health problems [70]. We have used both UV and visible light illuminations to analyse the photocatalytic performance of multiphase TiO$_2$ (TAB)-ZnO (ZW) nanostructure.

Before light illumination, the prepared multiphase nanostructure is kept under the dark condition for 1 hour to reach adsorption and desorption equilibrium. The degradation measurement is taken for different time intervals (0 to 180 min) with UV and visible light. The multiphase TiO$_2$ (TAB)-ZnO (ZW) nanoparticles showing enhanced degradation efficiency for methylene blue dye is due to its effective separation and generation of charge carriers. The multiphase combination is also favourable to increase the generation of photo induced electrons and holes by controlling the recombination of charge carriers. The photocatalytic mechanism of TiO$_2$ (TAB)-ZnO (ZW) mixed oxides is given as schematic diagram in Fig. 14 and equation 22 (a-e). Fig. 15 shows the absorption spectra of MB dye as a function of time in the presence of multiphase TiO$_2$ (TAB)-ZnO (ZW) nanostructure in both irradiation of UV and Visible light respectively. The absorption peak intensity of methylene blue dye under both UV and visible light shows the absence of new peaks at both the regions, and confirm the copious mineralization of MB molecules during the process. The methylene blue dye in aqueous solutions has the UV–Vis absorption maxima for monomer located at 668 and 624 nm, and oligomers (dimmer and trimmer) located at 606 nm and 565 nm, respectively with some overlapping [71]. The present study is in good agreement with these observations. The intensity of absorbance decreased intensively '661 nm for UV and Visible light illumination, confirming that MB monomer can be broken rapidly while its dimmer or trimmer being hard break at a slow rate due to the higher molar absorptivity. It takes longer time for its degradation. The degradation percentage is calculated using the absorption spectra with varying irradiation time [72]. The degradation efficiency is calculated using equation. (23).
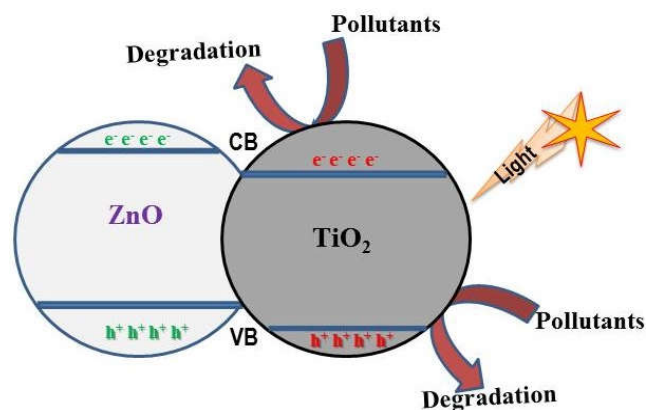
Fig. 14. Schematic representations of photocatalytic mechanism of TiO$_2$ (TAB)-ZnO (ZW) nanostructure as catalyst.
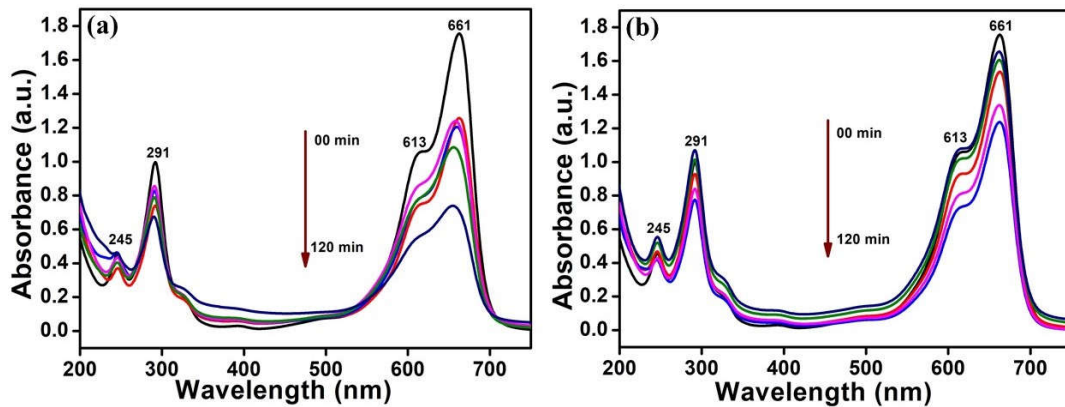
Fig. 15. Absorption spectral changes of methylene blue (MB) solution degraded by multiphase TiO₂ (TAB)-ZnO (ZW) nanoparticles: a) UV light. b) Visible light.

$$[TiO_2(AB) - ZnO(ZW)] + hv \rightarrow [TiO_2(AB) - ZnO(ZW)](e^- + h^+) \quad \text{(22a)}$$

$$[TiO_2(AB) - ZnO(ZW)](e^-) + O_2 \rightarrow [TiO_2(AB) - ZnO(ZW)] + O_2^{\bullet-} \quad \text{(22b)}$$

$$[TiO_2(AB) - ZnO(ZW)](h^+) + H_2O \rightarrow [TiO_2(AB) - ZnO(ZW)] + OH^{\bullet} \quad \text{(22c)}$$

$$O_2^{\bullet-} + MB \rightarrow \text{Degradation products} \quad \text{(22d)}$$

$$OH^{\bullet} + MB \rightarrow \text{Degradation products} \quad \text{(22e)}$$
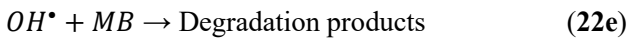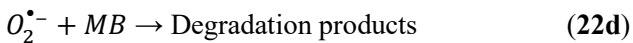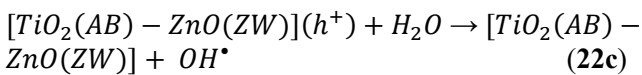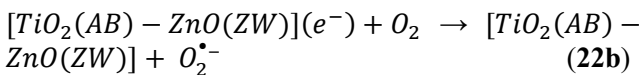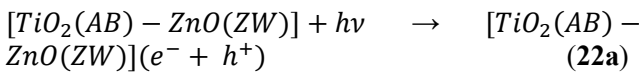
$$\text{Photodegradation (\%)} = \left[\frac{C_t - C_0}{C_0}\right] \times 100 \quad \text{(23)}$$

where; C_0 = absorption of before light irradiation, C_t= absorption of different time interval

Fig. 16 shows the dye concentration and degradation of the prepared mixed oxides with respect to time and different light irradiations. It shows that 97% degradation for UV light and 94% degradation for visible light are completed within 180 min. The results indicate that the unique optical, electronic, and catalytic properties of ZnO improve the photocatalytic behaviour, when coupled with TiO₂. The coupling of

two semiconductors of TiO₂–ZnO nanocomposite with different band gaps having different conduction and valence energy band levels allow the displacement of holes and electrons from one semiconductor to another. The degradation percentage of methylene blue dye in increased, due to the enhancement of the charge carrier separation, the accumulation of electrons/holes on the composite semiconductors with higher redox potential, and promotion of the electron transfer relative to the reduced charge carrier recombination of electron-hole pairs in the multiphase nanostructure. Adsorption of both the oxidant and the pollutant is a pivotal parameter in a heterogeneous photodegradation process. The degradation kinetics can be interpreted by the Langmuir–Hinshelwood (L-H) model only when the photodegradation is an equilibrium process. It is stated in equation (24) and it can be modified into the logarithmic form (equation 25) by integrating it. [73, 74].

$$r = \frac{-dc}{dt} = \frac{k'KC}{1+KC} = k'\theta \quad \text{(24)}$$

$$\ln\left(\frac{C_0}{C_t}\right) + k'(C_0 - C_t) = k'Kt = k_{app}t \quad \text{(25)}$$
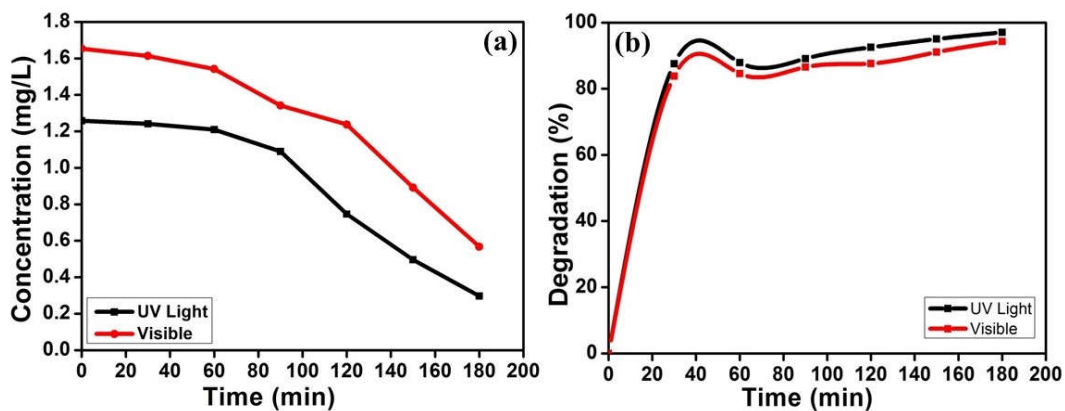
Fig. 16. Photocatalysis analysis: a) Dye concentration. b) Dye degradation of methylene.

where, r is the degradation rate of the reactant (mg/L min), C is concentration of the pollutant (mg/L), t is irradiation time, k' is specific reaction rate constant (mg/L min), K is equilibrium constant of the reactant (L/mg), C_0 is initial concentration, C_t is final concentration, and k_{app} is first-order rate constant, which is given by the slope of the graph: $\ln\left(\frac{C_0}{C_t}\right)$ versus time.

The graph (Fig. 17) plotted between $\ln(C_0/C_t)$ and irradiation time represents linear relationship which is in accordance with equation (23). The result clearly indicates that photodegradation of methylene blue (MB) follows first order kinetics and the rate constant is calculated for 0.0083, and 0.0052 min^{-1} for UV and visible light irradiation respectively. The higher photocatalytic activity of multiphaseTiO$_2$ (TAB)-ZnO (ZW) nanostructure in both UV and visible light illumination is due to the intimately bonded TiO$_2$ (TAB)-ZnO (ZW) heterostructure and reduced electron–hole recombination rate. The prepared multiphase structure enhances the degradation efficiency in visible region as well, which is due to the reduction of band gap of TiO$_2$ (TAB)-ZnO (ZW) multiphase nanostructure. The obtained degradation percentage and rate constants are given in Tables 4 and 5. The results obtained in the present study is compared with mono-phase and bi-phase structures of other reported works [25, 75-77], which are provided in the comparison Table (6). The obtained results indicate that the TiO$_2$ (TAB)-ZnO (ZW) multiphase mixed oxide nanoparticles can be used to degrade methylene blue dye (MB) for both UV and visible light irradiation.

4. Conclusions

Multiphase TiO$_2$ (TAB)-ZnO (ZW) nanostructure is synthesized using Sol-Gel route and is confirmed from XRD. The average crystallite size is calculated using Scherrer formula and the obtained average crystallite size is 33 nm. Also, the various physical parameters such as, crystallite size, strain, stress, and energy density are calculated using the Williamson-Hall model. The presence of oxides and functional groups are analysed with the help of FTIR spectroscopy. The peaks obtained at 342.79 and 679.44 cm^{-1} confirm the presence of TiO$_2$ and ZnO stretching modes in the prepared materials. The Raman spectrum confirms the presence of TiO$_2$ (TAB)-ZnO (ZW) nanostructure. The optical properties are studied using UV-Visible spectroscopy. The obtained absorption band edge is 308 nm and the calculated optical band gap is 3.1 eV. The spherical shape morphology is observed from FESEM. The particle size is also examined using DLS technique and

the obtained particle sizes are 433 and 97.32 nm. The Zeta potential analysis clearly reveals that the prepared multiphase TiO$_2$ (TAB)-ZnO (ZW) is more stable. The electrical properties are analysed using Impedance spectroscopy. The dielectric constant, dielectric loss, ac conductivity, and other electrical parameters such as resistance and capacitance due to grain boundaries are analysed. The results show that the prepared multiphase nanostructure exhibits good electrical properties. The binding energy and minimum hopping distance are calculated using impedance data and reveals that the prepared material is stable under different conditions. The photocatalytic behaviour of multiphase TiO$_2$ (TAB)-ZnO (ZW) catalyst is studied with two different light sources using methylene blue as the model dye. The higher degradation is achieved for both light illuminations and the obtained rate constant demonstrates the enhanced photodegradation of methylene blue (MB) dye.
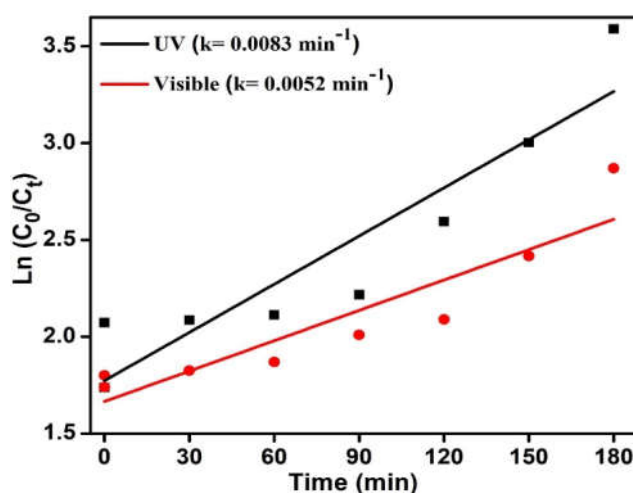
Fig. 17. Rate constant plot of ln (C$_0$/C$_t$) versus time

Table 4. Degradation of methylene blue (MB) dye with TiO$_2$ (TAB)-ZnO (ZW) semiconductor as catalyst

Time (min)	% Degradation		Ln (C$_0$/C$_t$)	
	UV light	Visible light	UV light	Visible light
0	87.42	83.47	2.0693	1.7974
30	87.58	83.86	2.0885	1.8268
60	87.90	84.58	2.1081	1.8725
90	89.10	86.58	2.2192	2.0057
120	92.54	87.62	2.5991	2.0860
150	95.04	91.08	3.3009	2.2652
180	97.24	94.33	4.1364	2.5156

Table 5. The rate constant (k), and Half life time ($t_{1/2}$).

Catalyst	Light illumination	Rate constant k (min^{-1})	Half-life $t_{1/2}$ (min)
TiO$_2$ (TAB)-ZnO (ZW)	UV	0.0083	83.49
	Visible	0.0052	133.27

Table 6. Comparison table for the rate constant (k) of the photocatalytic degradation of methylene blue dye.

Phase structure	Rate constant (k) (min^{-1})	Half-life time ($t_{1/2}$) (min)	Ref.
Anatase- TiO$_2$	0.0174	39.83	[75]
Anatase- TiO$_2$	0.0122	56.80	[76]
Wurtzite –ZnO	0.0035	198	[77]
Anatase+Rutile- TiO$_2$	0.0055	126	[76]
Anatase+Rutile- TiO$_2$	0.0074	93.65	[75]
Anatase+Rutile- TiO$_2$	0.0031	223.55	[25]
TARZW- multiphase structure	0.0045	154	[25]
TABZW- multiphase structure	0.0083, 0.0052	83.49, 133.27	Present work

Abbreviations

TiO2 (TAB)-ZnO (ZW)	TiO2 (Anatase + Brookite) – ZnO (Zinc wurtzite)
ZnO	Zinc Oxide
TiO$_2$	Titanium dioxide
TZ	Titanium dioxide/ Zinc Oxide
MB	Methylene Blue
XRD	X-ray Diffraction
FTIR	Fourier Transform Infrared Spectroscopy
UV-Vis	Ultraviolet Visible spectroscopy
FESEM	Field Emission Scanning Electron Microscopy
EDX	Energy Dispersive X-ray spectroscopy
DLS	Dynamic Light Scattering
IS	Impedance Spectroscopy

References

[1] M.R. Hoffmann, S.T. Martin, W. Choi, D.W. Bahnemann, Chem. Rev. 95 (1995) 69-96.

[2] M.-J. Jin, J. Jo, J.-W. Yoo, Org. Electron. physics, Mater. Appl. 19 (2015) 83-91.

[3] Y. Yang, G. Banerjee, G.W. Brudvig, J.H. Kim, J.J. Pignatello, Environ. Sci. Technol. 52 (2018) 5911-5919.

[4] O.M. Ishchenko, V. Rogé, G. Lamblin, D. Lenoble, Semicond. Photocatal. Mater. Mech. Appl. INTECH, 2016, pp. 3-30.

[5] N. Hafizah, I. Sopyan, Int. J. Photoenergy 2009 (2009) 1-8.

[6] D. Kanakaraju, S.P. Wong, J. Chem. 2018 (2018) 1-14.

[7] A. Mohammad Bagher, Am. J. Opt. Photonics. 3 (2015) 94.

[8] D. Zhou, T. Zhou, Y. Tian, X. Zhu, Y. Tu, J. Nanomater. 2018 (2018) 1-15.

[9] A. Ibhadon, P. Fitzpatrick, Catalysts. 3 (2013) 189-218.

[10] A. Dey, Mater. Sci. Eng. B. 229 (2018) 206-217.

[11] G. Korotcenkov, B.K. Cho, Sensors Actuators, B Chem. 244 (2017) 182-210.

[12] K. Wetchakun, T. Samerjai, N. Tamaekong, C. Liewhiran, C. Siriwong, V. Kruefu, A. Wisitsoraat, A. Tuantranont, S. Phanichphant, Sens. Actuators B Chem. 160 (2011) 580-591.

[13] M.R. Delsouz Khaki, M.S. Shafeeyan, A.A.A. Raman, W.M.A.W. Daud, J. Mol. Liq. 258 (2018) 354-365.

[14] L. Wang, X. Fu, Y. Han, E. Chang, H. Wu, H. Wang, K. Li, X. Qi, J. Nanomater. 2013 (2013) 1-6.

[15] N. Kamarulzaman, M.F. Kasim, R. Rusdi, Nanoscale Res. Lett. 10 (2015) 1034.

[16] S. Talam, S.R. Karumuri, N. Gunnam, ISRN Nanotechnol. 2012 (2012) 1-6.

[17] Y. Wang, Y.Z. Zheng, S. Lu, X. Tao, Y. Che, J.F. Chen, ACS Appl. Mater. Interfaces 7 (2015) 6093-6101.

[18] H. Yan, X. Wang, M. Yao, X. Yao, Prog. Nat. Sci. Mater. Int. 23 (2013) 402-407.

[19] C. Dette, M.A. Perez-Osorio, C.S. Kley, P. Punke, C.E. Patrick, P. Jacobson, F. Giustino, S.J. Jung, K. Kern, Nano Lett. 14 (2014) 6533-6538.

[20] Y. Wang, R. Zhang, J. Li, L. Li, S. Lin, Nanoscale Res. Lett. 9 (2014) 46.

[21] S. Anandan, Y. Ikuma, K. Niwa, Solid State Phenom. 162 (2010) 239-260.

[22] C. Cheng, A. Amini, C. Zhu, Z. Xu, H. Song, N. Wang, Sci Rep. 4 (2014) 4181.

[23] S. Moradi, P. Aberoomand-Azar, S. Raeis-Farshid, S. Abedini-Khorrami, M.H. Givianrad, J. Saudi Chem. Soc. 20 (2016) 373-378.

[24] D.L. Liao, C.A. Badour, B.Q. Liao, J. Photochem. Photobiol. A Chem. 194 (2008) 11-19.

[25] B.M. Rajbongshi, S.K. Samdarshi, B. Boro, J. Mater. Sci. Mater. Electron. 26 (2014) 377-384.

[26] R. Verma, J. Gangwar, A.K. Srivastava, RSC Adv. 7 (2017) 44199-44224.

[27] R. Daghrir, P. Drogui, D. Robert, Ind. Eng. Chem. Res. 52 (2013) 3581-3599.

[28] I. Ganesh, A.K. Gupta, P.P. Kumar, P.S. Sekhar, K. Radha, G. Padmanabham, G. Sundararajan, Sci. World J. 2012 (2012) 127326.

[29] R. Janisch, P. Gopal, N.A. Spaldin, J. Phys. Condens. Matter. 17 (2005) R657-R689.

[30] J. Maragatha, S. Rajendran, T. Endo, S. Karuppuchamy, J. Mater. Sci. Mater. Electron. 28 (2016) 5281-5287.

[31] A. Shokuhfar, A. Hassanjani-Roshan, M.R. Vaezi, S.M. Kazemzadeh, A. Esmaielzadeh Kandjani, B. Nasiri-Tabrizi, J. Nano Res. 11 (2010) 35-38.

[32] E. Peter Etape, L. John Ngolui, J. Foba-Tendo, D.M. Yufanyi, B. Victorine Namondo, J. Appl. Chem. 2017 (2017) 1-10.

[33] T. Tani, L. Mädler, S.E. Pratsinis, J. Nanoparticle Res. 4 (2002) 337-343.

[34] M.S. Lassoued, A. Lassoued, S. Ammar, A. Gadri, A.B. Salah, S. García-Granda, J. Mater. Sci. Mater. Electron. 29 (2018) 8914-8922.

[35] A.E. Shalan, A. Mourtada Elseman, M. Rasly, M.M. Moharam, M. Lira-Cantu, M.M. Rashad, RSC Adv. 5 (2015) 103095-103104.

[36] D.V. Aware, S.S. Jadhav, Appl. Nanosci. 6 (2015) 965-972.

[37] N. Hellen, H. Park, K.-N. Kim, J. Korean Ceram Soc. 55 (2018) 140-144.

[38] S. Lee, I.-S. Cho, J.H. Lee, D.H. Kim, D.W. Kim, J.Y. Kim, H. Shin, J.-K. Lee, H.S. Jung, N.-G. Park, K. Kim, M.J. Ko, K.S. Hong, Chem. Mater. 22 (2010) 1958-1965.

[39] D.P. Macwan, P.N. Dave, S. Chaturvedi, J. Mater. Sci. 46 (2011) 3669-3686.

[40] P. Vlazan, D.H. Ursu, C. Irina-Moisescu, I. Miron, P. Sfirloaga, E. Rusu, Mater. Charact. 101 (2015) 153-158.

[41] R. Bashiri, N.M. Mohamed, C.F. Kait, Recent Applications in Sol-Gel Synthesis, Rijeka: In Tech, 2017, pp. 151-167.

[42] S. Ramesh, J. Nanosci. 2013 (2013) 1-8.

[43] F.X. Xiao, ACS Appl. Mater. Interfaces. 4 (2012) 7055-7063.

[44] J. Mani, H. Sakeek, S. Habouti, M. Dietze, M. Es-Souni, Catal. Sci. Technol. 2 (2012) 379-385.

[45] H. Esteban Benito, T. Del Ángel Sánchez, R. García Alamilla, J.M. Hernández Enríquez, G. Sandoval Robles, F. Paraguay Delgado, Brazilian J. Chem. Eng. 31 (2014) 737-745.

[46] T.A. Kandiel, L. Robben, A. Alkaim, D. Bahnemann, Photochem. Photobiol. Sci. 12 (2013) 602-609.

[47] M.B. Bahar Khodadadi, Iran. J. Catal. 6(1) (2016) 37-42

[48] M.R.P. Subhash Dharmraj Khairnar, Vinod Shankar Shrivastava, Iran. J. Catal. 8 (2018) 143-150

[49] H.M. Chenari, C. Seibel, D. Hauschild, F. Reinert, H. Abdollahian, Mater. Res. 19 (2016) 1319-1323.

[50] B. Manikandan, T. Endo, S. Kaneko, K.R. Murali, R. John, J. Mater. Sci. Mater. Electron. 29 (2018) 9474-9485.

[51] T. Tamiji, A. Nezamzadeh-Ejhieh, J. Taiwan Inst. Chem. Eng. 104 (2019) 130-138.

[52] A. Seetharaman, S. Dhanuskodi, Spectrochim. Acta - Part A Mol. Biomol. Spectrosc. 127 (2014) 543-549.

[53] T.M.K. Thandavan, S.M.A. Gani, C.S. Wong, R.M. Nor, J. Nondestruct. Eval. 34 (2015) 14.

[54] S.J. Mofokeng, V. Kumar, R.E. Kroon, O.M. Ntwaeaborwa, J. Alloys Compd. 711 (2017) 121-131.

[55] M. Alijani, B.K. Kaleji, Opt. Quantum Electron. 49 (2017).

[56] A. León, P. Reuquen, C. Garín, R. Segura, P. Vargas, P. Zapata, P. Orihuela, Appl. Sci. 7 (2017) 49.

[57] K. Sowri Babu, A. Ramachandra Reddy, C. Sujatha, K. Venugopal Reddy, A.N. Mallika, J. Adv. Ceram. 2 (2013) 260-265.

[58] S. Dianat, Iran. J. Catal. 8(2) (2018) 121-132

[59] S. Nadzirah, U. Hashim, M. Kashif, S.A. Shamsuddin, Microsyst. Technol. 23 (2016) 1743-1750.

[60] J.F. Odah, International Letters of Chemistry, Int. Lett. Chem. Phys. Astron. 68 (2016) 71-81.

[61] S. Ghattavi, A. Nezamzadeh-Ejhieh, Desalin. Water Treat. 166 (2019) 92-104.

[62] M. Vahtrus, A. Šutka, S. Vlassov, A. Šutka, B. Polyakov, R. Saar, L. Dorogin, R. Lõhmus, Mater. Charact. 100 (2015) 98-103.

[63] A.-J. Cheng, Y. Tzeng, H. Xu, S. Alur, Y. Wang, M. Park, T.-h. Wu, C. Shannon, D.-J. Kim, D. Wang, J. Appl. Phys. 105 (2009) 073104.

[64] S. Yedurkar, C. Maurya, P. Mahanwar, Open J. Synth. Theory Appl. 05 (2016) 1-14.

[65] M. Mujahid, Bull. Mater. Sci. 38 (2015) 995-1001.

[66] G. Govindasamy, P. Murugasen, S. Sagadevan, Mater. Res. 19 (2016) 413-419.

[67] M. Mehedi Hassan, A.S. Ahmed, M. Chaman, W. Khan, A.H. Naqvi, A. Azam, Mater. Res. Bull. 47 (2012) 3952-3958.

[68] D.M.D.M. Prabaharan, K. Sadaiyandi, M. Mahendran, S. Sagadevan, Mater. Res. 19 (2016) 478-482.

[69] Y. Cherifi, A. Chaouchi, Y. Lorgoilloux, M. Rguiti, A. Kadri, C. Courtois, Process Appl. Ceram. 10 (2016) 125-135.

[70] D. Fungaro, L. Grosche, A. S. Pinheiro, J. Izidoro, S. Borrely, Orbital Electron. J. Chem. 2010, p. 235-247.

[71] S. Senobari, A. Nezamzadeh-Ejhieh, Spectrochim. Acta - Part A Mol. Biomol. Spectrosc. 196 (2018) 334-343.

[72] C. Chen, J. Liu, P. Liu, B. Yu, Adv. Chem. Eng. Sci. 01 (2011) 9-14.

[73] M.A.I. Molla, I. Tateishi, M. Furukawa, H. Katsumata, T. Suzuki, S. Kaneco, ChemEngineering 1 (2017) 8.

[74] N. Omrani, A. Nezamzadeh-Ejhieh, M. Alizadeh, Desalin. Water Treat. 162 (2019) 290-302.

[75] D.M. De Los Santos, J. Navas, T. Aguilar, A. Sanchez-Coronilla, C. Fernandez-Lorenzo, R. Alcantara, J.C. Pinero, G. Blanco, J. Martin-Calleja, Beilstein J. Nanotechnol. 6 (2015) 605-616.

[76] F.N. M. Z. B. Mukhlish, M. M. Rahman, M. J. Uddin J. Sci. Res. 5 (2013) 301-314.

[77] A. Phuruangrat, O. Yayapao, S. Thongtem, T. Thongtem, Russ. J. Phys. Chem. A. 90 (2016) 949-954.